Article

Evaluation of the Efficiency of Generation of Terahertz Surface Plasmon Polaritons by the End-Fire Coupling Technique

Vasily Valerievich Gerasimov [1,2,*] , **Alexey Konstantinovich Nikitin** [3], **Alexey Georgievich Lemzyakov** [2,4] **and Ivan Aleksandrovich Azarov** [1,5]

[1] Department of Physics, Novosibirsk State University, 630090 Novosibirsk, Russia; azarov_ivan@mail.ru

[2] Budker Institute of Nuclear Physics, Siberian Branch of the Russian Academy of Sciences, 11, Lavrentiev Prospect, 630090 Novosibirsk, Russia; a.g.lemzyakov@inp.nsk.su

[3] Scientific and Technological Centre of Unique Instrumentation, Russian Academy of Sciences, 15, Butlerova Street, 117342 Moscow, Russia; alnikitin@mail.ru

[4] Shared Research Center "Siberian Ring Photon Source", Boreskov Institute of Catalysis, Siberian Branch of the Russian Academy of Sciences, 1, pr. Nikolsky, 630559 Koltsovo, Russia

[5] Rzhanov Institute of Semiconductor Physics, Siberian Branch of the Russian Academy of Sciences, 13, Lavrentiev Aven., 630090 Novosibirsk, Russia

* Correspondence: v.gerasimov@nsu.ru

Abstract: One of the most important problems in the plasmonics of the terahertz (THz) range, which is actively developing now, is the efficient generation of surface plasmon polaritons (SPPs). The simplest and most promising technological technique of photon excitation of THz SPPs is through diffraction of radiation on the edge of the conducting surface of the sample (the end-fire coupling technique). In this paper, we experimentally evaluated the efficiency of the generation of monochromatic THz SPPs (λ_0 = 141 μm) by this method with a sample in the form of a cylindrical segment, the convex surface of which has a gold layer coated by zinc sulfide (ZnS) with thickness d = 0–2 μm. Such configuration of the surface supporting the SPPs not only shields the detector from parasitic bulk waves arising during diffraction but also enables one to change the distribution of the SPP field in the air by varying the coating layer thickness d. On an uncoated gold surface, the SPP generation efficiency was $\eta \approx 20\%$. In the presence of a ZnS layer on the gold, the SPP generation efficiency gradually increased with d, reached the maximum ($\eta_{max} \approx 60\%$) at $d \approx 1$ μm, and then gradually decreased. Theoretical analysis showed that the efficiency of the SPP generation can be raised up to 80% due to the selection of an optimal SPP field profile via variation of the thickness of the dielectric layer on the metal surface, as well as with optimal incidence of the focused radiation on the edge of the sample.

Keywords: surface plasmon polaritons; terahertz region; coupling efficiency; thin layers; integrated optics

1. Introduction

Surface plasmon polaritons (SPPs) are non-radiating surface electromagnetic waves guided by materials with negative permittivity [1,2]. The nature and properties of SPPs of the visible and mid-IR ranges, as well as their use for control of the surface and processes on it, have been studied quite well and have found wide application in optics [3,4], unlike SPPs of the terahertz (THz) range. The practical mastering of the THz range began only in the second half of the last century with the creation of laser sources (gas, free electron, semiconductor, and broadband pulsed) [5] and sensitive detectors (thermal, photonic, pyroelectric, photoconductive antennas, etc.) of THz radiation [6].

Calculations performed by the Drude model for the permittivity of metals show a very small difference between the THz SPPs and plane electromagnetic waves in the medium adjoining the metal. For example, on a flat homogeneous interface between a

high-conductivity metal (Au, Ag, Cu, Al, and Pt) and vacuum (dry air), the calculated propagation length L of THz SPPs is as large as tens and even hundreds of meters, and their phase and group velocities are less than the speed of light by only a few thousandths of a percent [7–9].

Such properties of THz SPPs demonstrate their potential for use in communication devices (to increase the speed of signal transmission) and devices for optical information processing. However, the first experiments on the excitation of THz SPPs by laser radiation (λ_0 = 118.8 μm) have already shown that on the sputtered and polished surfaces of the abovementioned metals, the L value does not exceed decimeters, i.e., is 2–3 orders of magnitude less than the calculated one, and the phase velocity differs from the speed of light not by a few thousandths, but by a few tenths of a percent [7,10,11]. The main reasons for this were found to be (1) the presence of inhomogeneities and roughness on the surface (which leads to the appearance of radiative losses of SPPs) [12,13]; (2) the difference between the permittivity of the near-surface layer of the metal (skin layer) and that in the depth of the metal [14]; (3) scattering of SPPs on the metal granules in the near-surface layer [15]; and (4) incorrectness of application of the Drude model in the THz range because of the weakly anomalous skin effect when the mean free path of conduction electrons exceeds the depth of the skin layer (decreasing with increase in the radiation wavelength λ_0); thus, the electrons carry away energy deep into the metal, which is not taken into account by the classical electrodynamics [16]. In addition, a certain contribution to the attenuation of SPPs is made by their thermal losses due to the skin effect and absorption of THz radiation by the water vapor in air.

Nevertheless, THz SPPs are effectively used for spectroscopy of subwavelength layers on a conducting surface when reflectometry methods are inefficient because of the high reflectivity of metals at THz frequencies [17]. There are a number of publications on the use of THz SPPs in metal surface refractometry [18–20], interferometry [21,22], semiconductor-heterostructure light emitters [23–25], photodetectors [26,27], and sensor devices [28–30], as well as in devices for control of THz SPP beams [9,31,32]. In addition, it turned out that the propagation length of THz SPPs over a real metal surface (with roughness and impurities) can be made several times larger due to the application to it of a layer of a non-absorbing dielectric of a certain thickness (the presence of the layer leads to decrease in the radiative losses of SPPs and protects the metal from external influences) [33].

According to most researchers in the field of THz plasmonics, one of the most topical problems is the conversion of the source radiation into SPPs. As known, for realization of this problem, it is necessary to fulfill the laws of conservation of energy and momentum for the bulk and surface waves. For the satisfaction of the first of the laws, the frequencies ω of these waves must be equal and satisfy the condition $\omega \leq \omega_{\mathrm{p}}/\sqrt{2}$ (where ω_{p} is the plasma frequency of the metal). The momentum conservation law is satisfied when the tangential components of the wave vector of the radiation incident on the surface and the SPP wave vector are equal [1–3]. While it is relatively easy to select a radiation source for a given metal, the wave vectors can be matched in only two ways: either by the method of attenuated total internal reflectance (ATR) or through the diffraction of the bulk wave on one or another inhomogeneity on the surface itself (planar diffraction grating, roughness, foreign inclusion, groove, etc.) or on an edge of an object placed in the medium (screen edge or prism edge) within the depth of penetration of the SPP field into it.

The ATR method is applicable if the SPP propagation length L is comparable to or less than the radiation wavelength λ_0 and there is no necessity for the generation of SPPs with field distribution unperturbed by the coupling element. Therefore, the ATR method is used mainly in the visible range, in which the radiation frequency ω for metals is slightly less than $\omega_{\mathrm{p}}/\sqrt{2}$ [34], which meets the abovementioned conditions. In the infrared and THz ranges, the radiation frequency is much lower than the plasma frequency of metals ($\omega \ll \omega_{\mathrm{p}}/\sqrt{2}$), and therefore SPPs are similar in their characteristics to a plane wave: the L value is as large as thousands of λ_0, and the depth of field penetration into the medium is expressed in centimeters [9]. Moreover, for large-wavelength SPPs, as well as for

plane waves, the diffraction effects become more and more pronounced with increasing λ_0. Therefore, if the ATR method is used for the excitation of large-wavelength SPPs when the optical coupling of the SPPs and the prism on its edge is broken because of the diffraction of the SPP field on the edge, a high-power fan of parasitic bulk waves arises, which leads to large energy losses and unacceptably low efficiency of the conversion of the source radiation into SPPs on the prism-free surface of the metal.

Thus, for photon generation of terahertz SPPs on the surface of noble metals, only the phenomenon of diffraction is used and implemented with one or another technology.

The classical elements utilized for this purpose are planar diffraction gratings formed on the surface supporting the THz SPP propagation [35–37]. To minimize radiative losses during the propagation of SPPs over the grating, the size of the grating (in the plane of incidence) must not exceed the diameter of the incident beam. Alternatively, the beam is directed to a grating portion adjacent to the flat surface of the sample under study (usually, the grating is deposited on a separate substrate adjacent to a flat face of the sample) [38]. The presence of a dielectric coating of subwavelength thickness on the grating makes it possible to reduce SPP losses because of re-emission into the medium [36]. The main advantage of grating coupling elements, in addition to their high efficiency, is their planarity, which enables the creation of compact devices. Their frequency and spatial selectivity in relation to the radiation to convert (applied in selective photodetectors [39,40]) is a limitation in the generation of broadband SPPs. The disadvantages of the grating method include the need to create a grating on the sample surface and significant diffraction losses during the transition of SPPs from the corrugated surface area to the plain one, which hinders the practical use of SPPs in the THz range.

Often, for excitation of IR and THz SPPs on a flat surface, the focused source radiation (monochromatic or broadband) is directed to the edge of a solid-state screen (aperture method) placed near the metal surface within the depth of the SPP field penetration into the medium (air) [9,41]. Diffracting on the edge, the incident radiation generates a set of plane waves the tangential components of the wave vector of which differ in the absolute value. Since the spectrum of the wave vectors of SPPs (even generated by monochromatic radiation) on a real surface has a certain width [42]; some of the diffracted plane waves and components of the SPP spectrum satisfy the momentum conservation law, which leads to the excitation of SPPs. Of course, the efficiency of conversion of radiation into SPPs is low in this case (a few percent [9,41]). However, screen coupling elements are non-selective (neither in frequency nor in the angle of incidence of radiation), which enables their use for the generation of broadband SPPs by picosecond pulses [43,44] or by radiation from heat sources [45]. Such elements have an obvious disadvantage of non-planarity and an advantage of contactlessness. Note also that in the so-called "two-prism" scheme for the measurement of the propagation length of IR and THz SPPs, the conversion of radiation into SPPs and vice versa occurs mainly due to the diffraction of the source radiation or the SPP field on an edge of the input or output prism, not due to ATR phenomena [9,46].

The method of diffraction of radiation on an edge (more rarely on a slot or groove) of the SPP support surface (the end-fire coupling technique) [47] possesses the main advantages (planarity, ease of implementation, large bandwidth, contactlessness, and compactness of the coupling element) of the abovementioned technological methods of photon excitation of THz SPPs. The calculated value of the coupling efficiency by this method in the visible and near-IR ranges is as high as $80 \div 95\%$ [47–49]. The use of the end-fire coupling technique is possible at THz frequencies as well [32,50].

A common drawback of all the abovementioned methods for conversion of a bulk THz radiation into SPPs is the generation of intense parasitic bulk waves, both from the diffraction of the incident radiation and from the scattering of SPPs on surface roughness and optical inhomogeneities [33]. Most of these waves are near-surface ones, and thus they create strong flare light to a photodetector placed near the surface of the sample under study. One of the simplest and most efficient methods of shielding from such flare light is the spatial separation of SPPs and parasitic bulk waves by coupling elements (for

conversion both of the source radiation into SPPs and of SPPs into the bulk wave to detect) with a convex cylindrical surface capable of supporting SPPs [51].

This article describes a technique for determination of the efficiency of SPP generation by the end-fire coupling method with the use of a coupling element in the form of a cylindrical segment, both in a "metal-vacuum" structure and in the presence of the metal of a non-absorbing dielectric layer of subwavelength thickness. Experiments on the approbation of the technique with the radiation ($\lambda_0 = 141$ μm) of the Novosibirsk free electron laser are described.

2. Theoretical Evaluation of the SPP Coupling Efficiency

Let us consider a focused *p*-polarized bulk wave with a Gaussian profile of the electric field vector

$$E_z^{inc}(y,z) = E_0 \cdot \exp\left(-\frac{y^2 + (z - z_0)^2}{w_0^2}\right) \cdot \exp(ik_0\psi), \tag{1}$$

where w_0 is the waist of the beam and $k_0 = 2\pi/\lambda_0$ is the wavenumber of the source radiation incident along the ψ axis on the rectangular edge of the conducting sample (Figure 1); the center of the radiation beam is at the distance z_0 from the metalized surface of the sample. In our case, the surface is metalized by an opaque gold layer 300 nm thick, over which a zinc sulfide (ZnS) layer of thickness d is deposited. The sample is in air with the dielectric permittivity $\varepsilon_a \approx 1.0005$ [52].
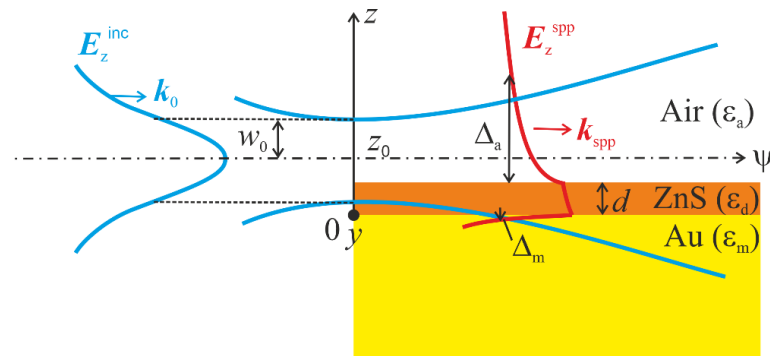

Figure 1. Scheme for evaluation of the SPP coupling efficiency at the diffraction of a focused Gaussian beam on a sample edge.

Because of the diffraction of the incident wave on the edge of the sample, surface plasmon polaritons (SPPs) are excited in the Au-ZnS-air structure and propagate along it. The longitudinal component (along the ψ *axis*) of the wave vector of the incident wave should be maximal (i.e., equal to k_0) to be as close as possible to the SPP wave vector k_{spp}. This is achieved in the region of the focused beam waist, where the beam wavefront is quasi-flat. In this case, the small difference between k_{spp} and k_0 ($(k_{spp}/k_0 - 1) << 1$) is compensated for at the diffraction of the radiation on the edge of the sample, which leads to the matching of the wave vectors of the incident and surface waves, which is necessary for the generation of SPPs. In this case, the efficiency of SPP generation depends mainly on the overlap ("matching") of the fields E_z (z,y) of the incident and surface waves [53].

Solving the wave equation for the three-layer structure ("Metal–Dielectric layer–Air") subject to the boundary conditions for the tangential components of the magnetic (H_y^{spp}) and electric (E_x^{spp}) fields gives the following solution for the z component of the electric field vector of the SPPs E_z (z,y) [54]:

$$E_z^{spp}(y,z) = E_{0z}^{spp} \cdot \exp\left(-\frac{y^2}{w_0^2}\right) \exp(ik_{spp}\psi) \begin{cases} \frac{\tilde{n}_{spp}}{\varepsilon_m} \cdot \exp(\gamma_m z), \, z \leq 0 \\ \frac{\tilde{n}_{spp}}{\varepsilon_d} \cdot \left(sh(\gamma_d z) + \frac{\gamma_m}{\gamma_d}\frac{\varepsilon_d}{\varepsilon_m}ch(\gamma_d z)\right), \, 0 \leq z \leq d \\ \frac{\tilde{n}_{spp}}{\varepsilon_a} \cdot \left[sh(\gamma_d d) + \frac{\gamma_m}{\gamma_d}\frac{\varepsilon_d}{\varepsilon_m}ch(\gamma_d d)\right] \cdot \exp(-\gamma_a(z - d)), \, d \leq z \end{cases}, \tag{2}$$

where E_{0z}^{spp} is the amplitude of the z component of the SPP electric field; $\gamma_m = k_0\sqrt{\tilde{n}_s^2 - \varepsilon_m}$, $\gamma_d = k_0\sqrt{\tilde{n}_s^2 - \varepsilon_d}$, and $\gamma_a = k_0\sqrt{\tilde{n}_s^2 - \varepsilon_a}$ are the constants of the SPP field attenuation in the metal, dielectric, and air, respectively; ε_m, ε_d, and ε_a are the permittivities of the respective media; and $\tilde{n}_s = n_s + i \cdot \kappa_s$ is the complex refractive index of the SPPs.

Using reference experimental data for the wavelength $\lambda_0 = 141$ μm for ZnS ($\varepsilon_d = 8.66 + i \cdot 0.059$, [55]) and the effective permittivity of the deposited gold surface ($\varepsilon_m = -7000 + i \cdot 3000$), identified within the SPP penetration into the metal [56], we calculated the dependences of the depth of the SPP field penetration into metal $\Delta_m = 1/\gamma_m$ (Figure 2a) and air $\Delta_a = 1/\gamma_a$ on the thickness d of the ZnS coating (Figure 2b) by numerical solution of SPP dispersion equation for three-layer structure. For comparison, the black lines in this figure show the similar dependences calculated for the permittivity $\varepsilon_m = -104700 + i \cdot 317180$, found by the Drude model for crystalline gold [57]. It can be seen that Δ_m for the deposited gold surface was five times larger than that for the crystalline metal and does not depend on the ZnS layer thickness. Δ_a for gold with the surface permittivity was noticeably smaller than that for the crystalline metal; moreover, for gold without the ZnS layer ($d = 0$), this difference was almost one order of magnitude. These facts should be taken into account in the search for the optimal conditions for the generation of THz SPPs. Subsequently, all calculations were carried out with the effective permittivity of the deposited gold surface.
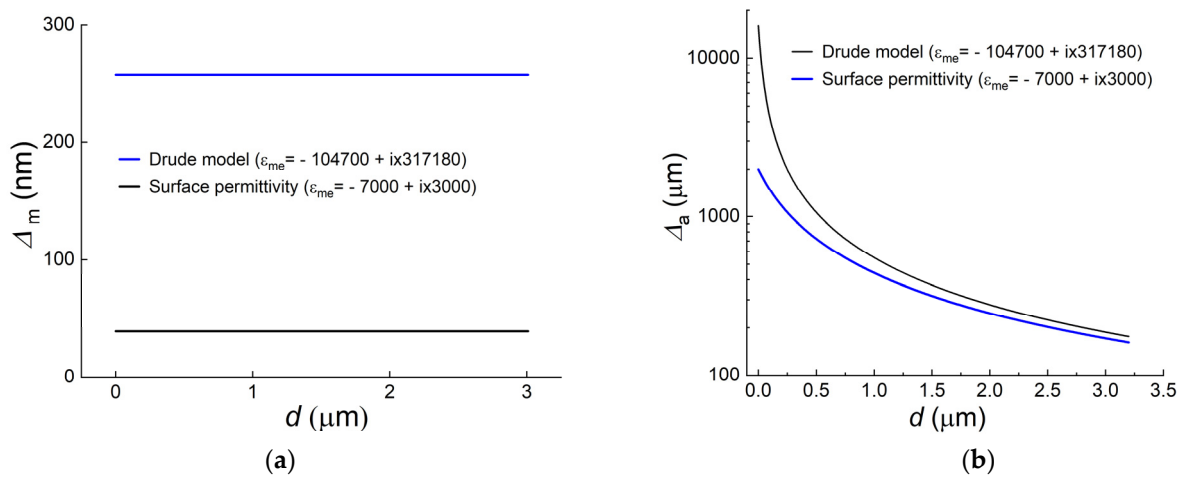

Figure 2. Depth of SPP field penetration into metal (**a**) and air (**b**) Δ_a for the "Au–ZnS layer–Air" structure vs. layer thickness d, obtained by numerical solution of SPP dispersion equation for three-layer structure at wavelength $\lambda_0 = 141$ μm with use of the permittivity of gold calculated by Drude model (black lines) and experimentally found for the surface of the deposited gold [56] (blue lines).

Using Formulas (1) and (2) and taking into account the normalization, we calculated the distributions of the incident radiation field E_z^{inc} (z) (at $z_0 = 0$) with $w_0 = 450$ μm, found experimentally (see Appendix A), and the surface wave field E_z^{spp} (z) at different thicknesses of the ZnS coating (Figure 3). As can be seen from Figure 3a, the SPP field E_z^{spp} penetrates into the metal ($z < 0$) to a very small depth ($\Delta_m = 1/\gamma_m \approx 250$ nm), decreases a little in the dielectric ($0 < z < d$), and exponentially decays in the air ($z > d$) at a distance of the hundred micrometers (Figure 3b).
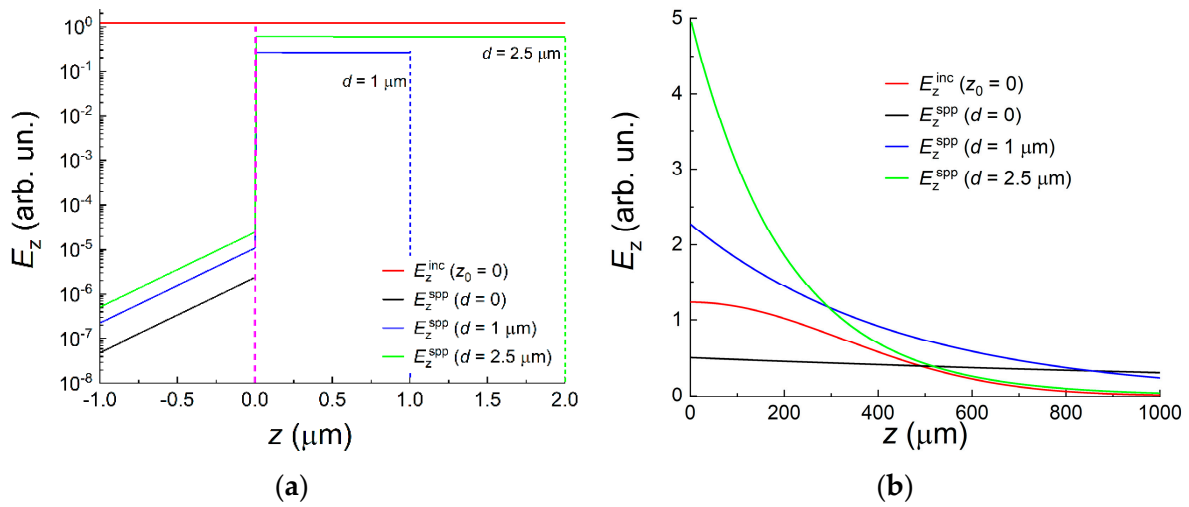
Figure 3. Distribution of the focused radiation field E_z^{inc} (z) at the distance to sample surface $z_0 = 0$ and the SPP field E_z^{spp} (z) at the ZnS coating layer thicknesses $d = 0$, 1.0, and 2.5 μm: (**a**) -1 μm $< z <$ d; (**b**) $d < z$.

Order of Several

At the transition of the metal–dielectric ($z = 0$) and dielectric–air ($z = d$) interfaces, the field component E_z^{spp} experiences a jump due to the concentration of the electric charge on the metal surface, which causes SPP propagation over the conductor surface [54].

It can be seen in Figure 3a that the field E_z^{spp} in the metal is several orders of magnitude smaller than the field in the dielectric layer or air, which indicates weak coupling of the SPPs with the metal surface and small Joule losses in the metal. With the increase in the thickness d of the coating layer, the field E_z^{spp} in the air is confined to the surface of the sample (the depth Δ_a of penetration of the SPP field into the air decreases; see Figure 2), and its intensity near the metal surface and inside the metal grows, which leads to increase in the Joule losses of the SPPs.

The efficiency of conversion of the incident wave energy into the surface wave energy is governed by the overlap ("matching") of the fields of these waves, and, as can be seen from Figure 3a,b, must strongly depend both on the coating thickness d and on the value of z_0. When the beam center goes below the level of the metal surface ($z_0 < 0$), the coupling efficiency is expected to decrease, and with an increase in z_0 in the region of its positive values, it is expected to rise. To understand this in detail, we calculated the coupling efficiency η of the incident bulk wave into SPPs using the classical expression [58]

$$\eta = \frac{\left| \iint E_z^{\text{inc}}(y,z) \cdot E_z^{\text{spp}}(y,z) \, dy \, dz \right|^2}{\iint \left| E_z^{\text{inc}}(y,z) \right|^2 dy \, dz \cdot \iint \left| E_z^{\text{spp}}(y,z) \right|^2 dy \, dz} = \frac{\left| \int\limits_0^\infty E_z^{\text{inc}}(z) \cdot E_z^{\text{spp}}(z) \, dz \right|^2}{\int\limits_{-\infty}^\infty \left| E_z^{\text{inc}}(z) \right|^2 dz \cdot \int\limits_0^\infty \left| E_z^{\text{spp}}(z) \right|^2 dz}, \quad (3)$$

where the integration with respect to the y coordinate yields unity because the profiles of the incident wave and the surface wave along the y-axis coincide. The numerator of expression (3) contains the overlap integral of the fields of the incident wave and SPPs, and the denominator contains their intensity.

Using Expressions (1)–(3), we calculated the dependence of the SPP generation efficiency η on the thickness d of the ZnS coating for some positions z_0 of the central part of the incident beam in the range from -200 μm to 800 μm (Figure 4a). With an increase in d, almost all curves first showed growth of the η value, which reached its maximum at a certain thickness d of the ZnS layer and then gradually decreased. Figure 4b shows the dependence of the efficiency on the position of the central part of the incident beam $\eta(z_0)$.

Like the dependence $\eta(d)$, $\eta(z_0)$ had a maximum, but at a certain z_0. Thus, it can be stated that there is an optimal thickness d of the coating layer and a position z_0 of the incident beam at which the efficiency of the conversion of the incident wave into SPPs will be the highest, which is due to the maximum overlap of the fields of the bulk and surface waves (see Figure 3b).
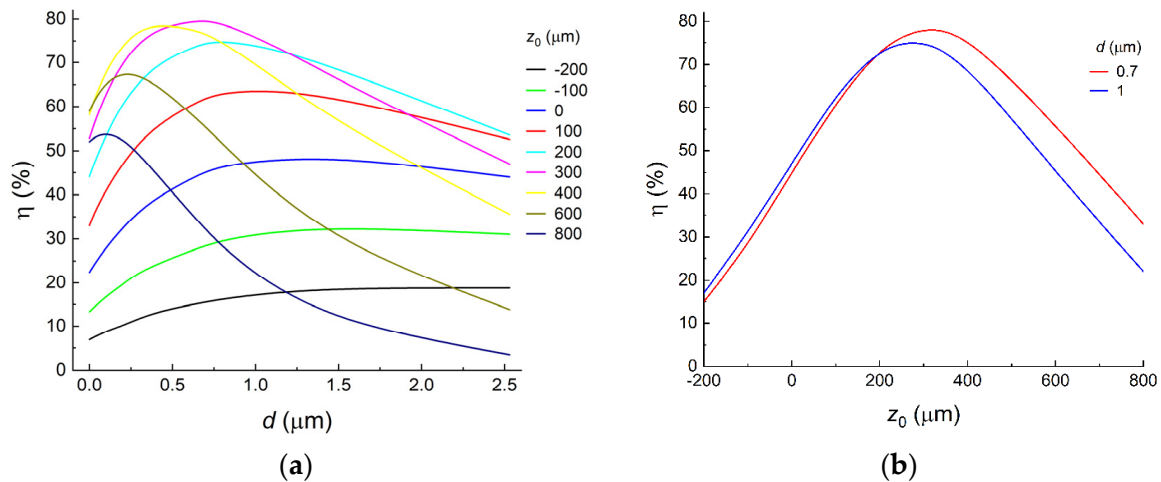

Figure 4. SPP generation efficiency η vs. (**a**) thickness d of ZnS layer deposited on the gold surface, calculated for several values of coordinates z_0 of the central part of the incident radiation beam, and (**b**) position of the central part of incident beam z_0 for the ZnS coating thickness d = 0.7 and 1 μm.

According to Figure 4, the maximum efficiency of THz SPP generation in the example under consideration is $\eta \approx 80\%$, which is comparable to the maximum achieved efficiency in the visible and IR ranges (80–95%, [47–50]). The efficiency of SPP generation can be raised even more if the incident wave profile shape is made as close as possible to the SPP field distribution. Among the available works on the evaluation of the efficiency of generation of SPPs by the end-fire coupling technique in the THz range, the highest calculated efficiency on bare metal with a dielectric waveguide as a coupling element was about 46% [59]. Note that the abovementioned estimate of the SPP coupling efficiency was obtained under the condition of approximate equality of the wave vectors, $k_{\mathrm{spp}} \approx k_0$. With increase in the thickness of the coating layer, the difference between the vectors k_{spp} and k_0 becomes significant, which leads to the growth of the energy losses of the incident wave in the scattering on the edge of the sample and a corresponding decrease in the efficiency of SPP generation. In addition, in our calculations, it was assumed that the edge of the sample had an ideally rectangular shape, as well as even and smooth boundaries. The presence of irregularities on the edge and surface of real samples leads to additional growth of the diffraction energy loss of the incident wave [53].

3. Experimental Setup

One of the main difficulties in experimental evaluation of the efficiency of conversion of focused radiation into SPPs by the end-fire coupling technique on flat conducting surfaces is the presence of parasitic bulk waves, which inevitably arise because of both the diffraction on the edge of the sample and the radiative losses of SPPs on surface inhomogeneities. These bulk waves make a significant contribution to the detected signal, which distorts the measurement results. However, if samples with a convex surface are used, then both types of parasitic bulk waves can be spatially separated from SPPs, and the efficiency of SPP generation can be estimated more correctly. For this reason, in this work, we used samples with a cylindrical conductive surface, which were earlier studied in [51].

The scheme of the experiment is shown in Figure 5a. The terahertz Gaussian beam (Figure 5b) of the Novosibirsk free electron laser (NonoFEL) with a beam waist of 11 mm

and wavelength $\lambda_0 = 141$ μm was focused by a cylindrical mirror ($F = 80$ mm) on the edge of the cylindrical face of the sample, where part of the radiation energy was converted into SPPs because of diffraction. For achievement of the maximum efficiency of the SPP generation, the optical axis of the focused beam (according to Section 2) was directed tangentially to the surface of the cylinder at the generation site ($\theta = 0$), and the point of incidence of the beam was adjusted along the z-axis so that the intensity of the generated SPPs was maximal at a certain position z_0 of the center of the incident Gaussian beam with respect to the sample surface. The sample was one-eighth of a glass cylinder with a radius of 60 mm. Its optically polished convex surface has a coating of a magnetron-sputtered opaque layer of gold 0.3 μm thick, over which a uniform layer of zinc sulfide (ZnS) of some thickness d in the range from 0 to 2 μm was deposited in a single technological cycle by electron beam sputtering. The thicknesses of the ZnS coatings were measured at several points along the cylindrical samples with the "Spektr" ellipsometer, developed by the Institute of Semiconductor Physics SB RAS [60].
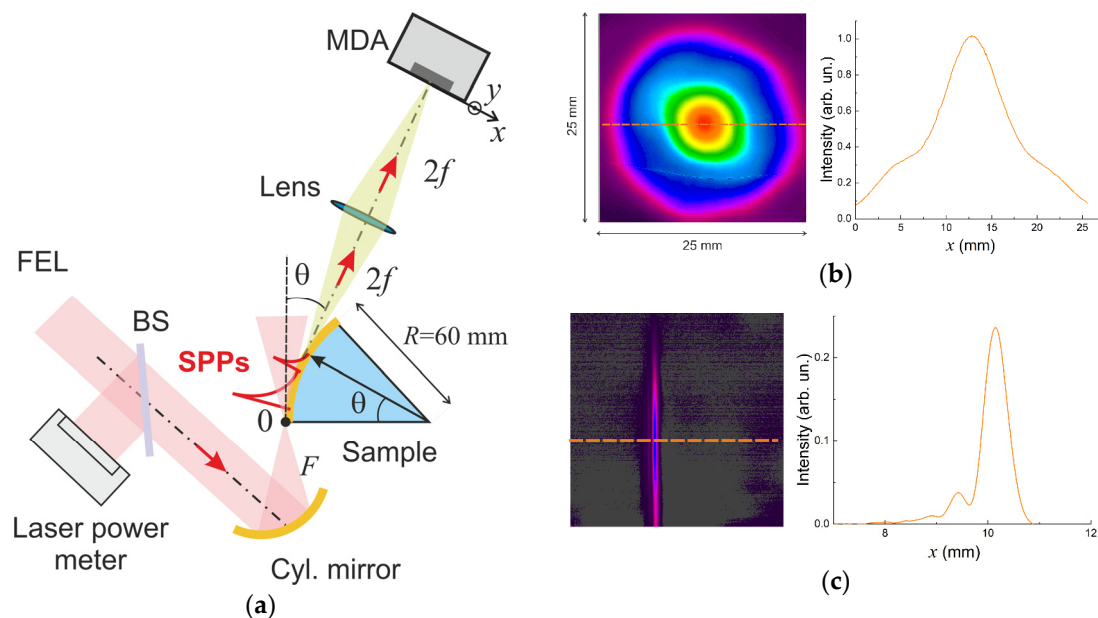

Figure 5. (**a**) Scheme of the experiment; (**b**) the intensity distribution in the cross-section of the THz beam incident on the cylindrical mirror; (**c**) the intensity distribution in the cross-section of the beam focused by the cylindrical mirror onto the sample edge. Images (**b**,**c**) were obtained with a pyroelectric detector array Pyrocam IV (Ophir photonics) with a sensitive area of 25×25 mm^2 (320×320 pixels).

Because of the curvature of the sample surface, the SPPs supported by it were converted with some efficiency into bulk waves, emitted tangentially to the surface into the surrounding space. This bulk radiation from the SPP track was detected with an imaging system consisting of a silicon (HRFZ) lens with focal length $f = 75$ mm and microbolometer detector array (MDA) [61,62], which were placed according to the $2f$-$2f$ scheme. The MDA contained 320×240 microbolometers, each of 51 μm in size (the size of the array was 16×12 mm^2). The angular distribution of the SPP intensity was recorded with a variation of the observation angle θ of the bulk waves breaking off the SPP track (the angle θ corresponded to the angular coordinate of the SPP break-off point). For recording the intensity distribution in cross sections of higher-power incident and focused beams (Figure 5b,c), we used the pyroelectric detector array Pyrocam IV (Ophir photonics), which is less sensitive to THz radiation and has a larger size of 25×25 mm^2 (320×320 pixels). In addition, unlike the MDA, the Pyrocam detector does not have an input window, which makes it possible to avoid multiple interference in it. For control of the NovoFEL power at the input

of the setup, part of the radiation was reflected from the beam splitter *BS* and recorded by the laser power meter.

Figure 6a shows an example of the intensity distribution in the cross-section of the beam of bulk waves breaking off the SPP track on a sample with a ZnS coating 0.75 μm thick at the observation angle θ = 27°, obtained with the imaging system. Figure 6b shows the profile of a cross-section of this distribution along the *x*-axis. The position of the sample surface corresponds to *x* = 0. On the right-hand side from the sample surface (*x* > 0), the signal has a complex profile of a series of maxima and minima, which turns into a gradual decrease in intensity. Such a pattern is associated with the interference of coherent waves breaking off the nearby portions of the SPP track, as well as with the multiple interferences in the germanium window of the detector array. Note that the bulk waves arising at the diffraction of the laser radiation incident on the sample edge could not get into the detector because at θ > 13° the detector was reliably shielded from them by the convex surface of the sample.
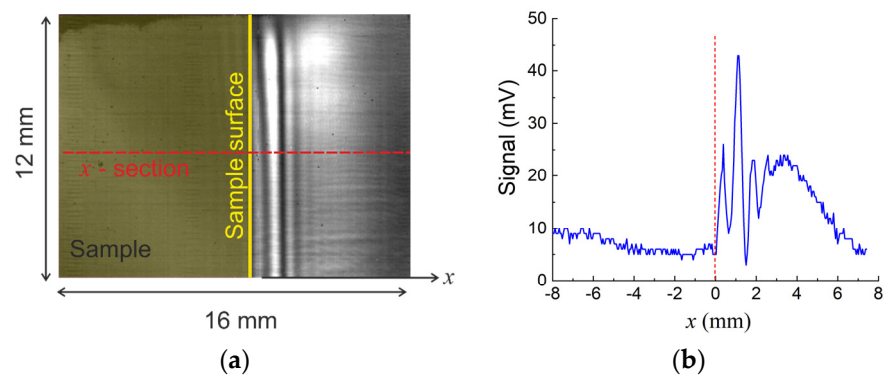

Figure 6. (**a**) Example of the intensity distribution in a cross-section of the beam of bulk waves breaking off the SPP track on a sample with a ZnS coating 0.75 μm thick at the observation angle θ = 27°; (**b**) profile of a cross-section of distribution along the x-axis.

Geometric estimates (see Appendix B) showed that the range of angles of incidence of bulk waves breaking off the SPP track onto the detector array is governed by the lens diameter *D* = 50 mm; it was $\Delta\theta \approx 20°$, which corresponded to the cylindrical surface segment $\Delta l = R \cdot \Delta\theta \approx 2$ cm. In this case, the radiation incident on the detector array illuminated only half of its detection area, and thus the total power $I_{\text{rad}}(\theta)$ of the radiation breaking off the segment Δl could be found via integration of the signal over all illuminated pixels of the detector.

4. Experimental Results and Analysis

According to the law of energy conservation, in the absence of non-linear interaction of the SPP field with the sample surface (which was so at the radiation power densities used in the experiments), the intensity of SPP radiation losses I^{rad} due to the curvature of the surface at a given angle θ of their detection is proportional to the energy of the surface wave, $I^{\text{rad}}(\theta) \sim I^{\text{SPP}}(\theta)$. Therefore, the rate of attenuation of the SPP intensity is equal to the rate of attenuation of the recorded signal:

$$\begin{array}{l} dI^{\text{SPP}}(\theta)/d\theta = -I^{\text{SPP}}(\theta) \cdot \alpha \cdot R, \\ dI^{\text{SPP}}(\theta)/d\theta = dI^{\text{rad}}(\theta)/d\theta \end{array} \quad , \tag{4}$$

where α is the coefficient of SPP attenuation during the SPP propagation over the cylindrical surface, and $dI^{\text{rad}}(\theta)/d\theta$ can be found from the measured dependence $I^{\text{rad}}(\theta)$.

Figure 7 shows the dependences $I^{\text{rad}}(\theta)$ measured with the detector array for samples with different thicknesses of the ZnS coating layer. The slope of the graphs is governed by

the coefficient α. Approximating these dependencies with an exponential function of the form

$$I^{\text{rad}}(\theta) = A \cdot \exp(-\alpha \cdot R \cdot \theta) + I_0, \tag{5}$$

where $R \cdot \theta$ is the path the SPPs propagate from the place of their generation (the edge of the convex surface of the sample) to the observation point, at which we found the coefficient α. The coefficient A at the exponent corresponded to the intensity of radiative losses at $\theta = 0^0$ and I_0 related to the background noise.
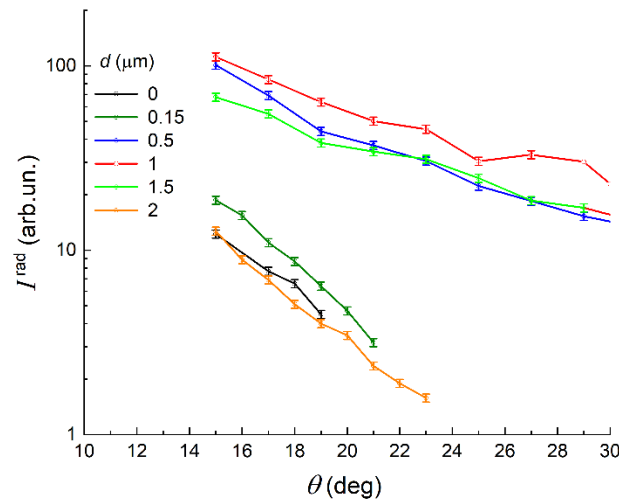
Figure 7. The intensity of bulk radiation from SPP track I^{rad} (radiative losses of SPPs) vs. observation angle θ. Data are presented for Au samples with a ZnS coating layer of thickness $d = 0$, 0.15, 0.5, 1.0, 1.5, and 2.0 μm.

The red circles in Figure 8a indicate the experimental values of α resulting from the approximation for different thicknesses d of the ZnS coating, and the blue circles in Figure 8b show the corresponding values of the coefficient A. For comparison, the blue dots in the graph (Figure 8a) show data from the previous experiments on the study of SPP propagation over cylindrical surfaces, performed with a lens-Golay cell imaging system (with a narrow slit at the entry) with its elements placed according to the 2f-2f scheme [51]. In that case, the samples were one-fourth parts of cylinders of the same radius $R = 60$ mm, their convex surface metalized with gold, in which the thickness of the ZnS coating was significantly inhomogeneous along the SPP track (because of shortcomings in the ZnS sputtering technology on the cylindrical surfaces), which led to additional radiative losses of SPPs. According to ellipsometric measurements, in the samples used in this work (segments of identical cylinders with an angle of 45° at the apex), the thickness uniformity of the ZnS layer was much better, as evidenced by the lower values of α (Figure 8a), especially so at $d > 1.0$ μm.

The experimental dependences $\alpha(d)$ presented in Figure 8a have minima, which are due to the competition between two types of SPP losses during the SPP propagation over the convex surface: (1) ohmic losses α_{joule} in the metal and (2) radiative losses α_{rad} arising both from the curvature of the surface and from surface inhomogeneities [33,51]. The total losses of SPPs are equal to the sum of these two types of losses:

$$\alpha = \alpha_{\text{joule}} + \alpha_{\text{rad}}, \tag{6}$$

On the one hand, as d increased, the ohmic losses rose because the surface wave energy fraction transferred in the metal was higher in the presence of a dielectric coating layer on the metal (see Figure 3a). On the other hand, as d increased, the radiative losses of SPPs decreased because the application of the dielectric layer to the metal leads, due to the higher SPP wave number k_{SPP}, to a larger distance between the SPP dispersion curve

from the light line in the graph of $k_{SPP}(\omega)$ (see Appendix C) and, consequently, to a lower probability of conversion of SPPs into bulk waves on the curvature and inhomogeneities of the surface [33]. Therefore, at a certain coating thickness $d_{\min}$, the total losses of SPPs α reached the minimum. Figure 8a shows that the minimum on the curve $\alpha(d)$ for the samples used in this work was reached at $d_{\min} \approx$ (1.0–1.5) μm when the SPP attenuation coefficient α decreased by a factor of 4 compared with the case of gold surface without a coating.

(a)

(b)
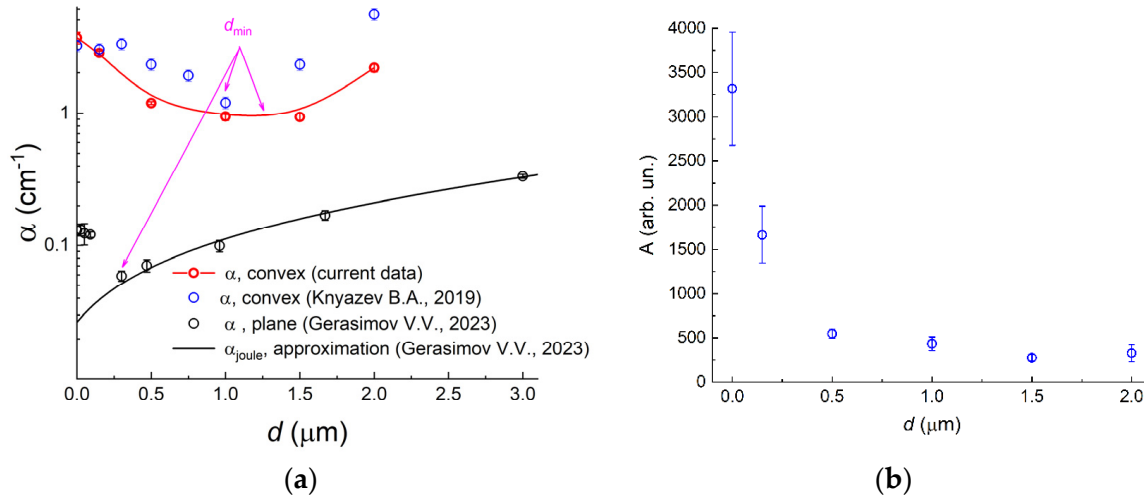
Figure 8. (**a**) SPP attenuation coefficient α vs. ZnS coating thickness d. Red dots: experimental values obtained in this work; blue dots: similar data from [51]; black dots: data on flat Au-ZnS-air surface from [56] with respective approximation black curve (from which effective permittivity of surface of sputtered gold was found), characterizing ohmic losses in gold and not taking into account radiative losses of SPPs on heterogeneities of flat surface. (**b**) Radiative loss coefficient A found by fitting experimental dependences shown in Figure 7.

For assessment of the ratio of the SPP losses during SPP propagation over flat and cylindrical surfaces (with R = 60 mm), the black dots in Figure 8a show the $\alpha(d)$ values obtained in experiments on gold surface refractometry [56]; the gold was deposited by the same technology on a polished flat glass surface. It can be seen that for the flat surface, the coefficient α was approximately an order of magnitude smaller than that for the cylindrical surface, which indicates the predominance of radiative losses on the curvature of the surface over the losses on the plane, the latter consisting of the ohmic losses in the metal and radiative losses on surface inhomogeneities. Note that for the flat surface, there was also a minimum of total SPP losses, but at a smaller thickness of the ZnS layer ($d_{\min} \approx 0.3$ μm) as compared with the cylindrical surface, which is due to the absence of radiative losses on the curvature.

The black solid curve in Figure 8a shows the dependence of the ohmic loss coefficient in the metal α_{joule} (d), found by approximation of the experimental dependence in [56]. These $\alpha_{\mathrm{joule}}(d)$ values corresponded to the effective permittivity of the sputtered gold surface ε_{m} = $-7000 + i\cdot3000$, which was approximately two orders of magnitude less than the crystalline metal permittivity calculated by the Drude model for λ_0 = 141 μm ($\varepsilon_{\mathrm{Drude}}$ = $-104700 + i\cdot317180$). It can be seen that at $d \approx 0$ μm, the ohmic losses α_{joule} of SPPs in the metal were an order of magnitude less than the radiative losses of SPPs on the flat gold surface without coating and approximately two orders of magnitude less than the total losses of SPPs on the metalized cylindrical surface.

From the graph in Figure 8b it can be seen that the coefficient A, which characterizes the radiative losses of SPPs at θ = 0, had the greatest value at d = 0, which is explained by the weak coupling of the SPPs with the bare metal (the depth of penetration of the SPP field into the air at d = 0 is maximal (see Figure 3b), and on the graph of $k_{SPP}(\omega)$, the SPP dispersion curve came closest to the light line (Appendix C). As d increased, the

radiative losses gradually decreased, which indicates improvement in the optical coupling of the SPPs with the sample surface (the SPP field is localized near the surface, and the SPP dispersion curve moves away from the light line).

5. Experimental Evaluation of SPP Coupling Efficiency

As SPPs propagate over the cylindrical surface, their intensity weakens as follows:

$$I^{\mathrm{spp}}(\theta) = I_0^{\mathrm{spp}} \cdot \exp(-\alpha \cdot R \cdot \theta), \tag{7}$$

where I_0^{spp} is the SPP intensity at the place of SPP generation at $\theta = 0$ (the values of the angle θ are in radians).

With Expressions (4) and (7), the attenuation rate of the intensity of the radiative losses recorded by the imaging system can be written in the following form:

$$\frac{dI_{\mathrm{rad}}}{d\theta} = -I_0^{\mathrm{spp}} \cdot \exp(-\alpha \cdot R \cdot \theta) \cdot \alpha \cdot R. \tag{8}$$

Integrating expression (8) over the observation angle of the detector array, i.e., from $\theta - \Delta\theta/2$ to $\theta + \Delta\theta/2$ (where $\Delta\theta \approx 20^\circ$, see Appendix B), we obtain

$$I_{\mathrm{rad}}(\theta) = I_0^{\mathrm{spp}} \cdot \left[\exp\left(\alpha \cdot R \cdot \frac{\Delta\theta}{2} \right) - \exp\left(-\alpha \cdot R \cdot \frac{\Delta\theta}{2} \right) \right] \cdot \exp(-\alpha \cdot R \cdot \theta) \cdot \tag{9}$$

According to (5), the coefficient at the exponent $I_0^{\mathrm{spp}} \cdot [\exp\left(\alpha \cdot R \cdot \frac{\Delta\theta}{2} \right) - \exp\left(-\alpha \cdot R \cdot \frac{\Delta\theta}{2} \right)] = A$. Therefore, one can find the intensity of SPPs at the place of SPP generation on the edge of the sample (for $\theta = 0$):

$$I_0^{\mathrm{spp}} = \frac{A}{\left[\exp\left(\alpha \cdot R \cdot \frac{\Delta\theta}{2} \right) - \exp\left(-\alpha \cdot R \cdot \frac{\Delta\theta}{2} \right) \right]} \tag{10}$$

Then the coupling efficiency of SPPs can be determined as

$$\eta = \frac{I_0^{\mathrm{spp}}}{I_0}, \tag{11}$$

where I_0 is the intensity of the radiation incident on the edge of the sample. The value $I_0 \approx 314$ (r. u.) was found by integration over the focal spot region recorded with the imaging system containing the MDA (see Figure 5a).

Figure 9 shows the $\eta(d)$ plot determined in this way. On the bare gold, the SPP coupling efficiency was $\eta \approx 20\%$. With a ZnS layer deposited on the gold surface, the SPP generation efficiency increased, reached the maximum ($\eta_{\max} \approx 60\%$) at $d \approx 1$ μm, and then gradually decreased. For comparison, this figure shows the theoretical dependences $\eta(d)$ calculated by Formulas (1)–(3) (see Figure 4a) for two values of z_0 (position of the central part of the incident beam with respect to the metal surface), which are in the best agreement with the experiment. It can be seen that at the ZnS layer thickness $0 < d < 1$ μm, there was good agreement between the experiment and theoretical estimates, and at $d > 1$ μm, the decrease in the experimental values of η was noticeably greater than that in theory. As noted in Section 2, the decrease in the coupling efficiency of SPPs at large thicknesses of the dielectric coating can be caused by the larger difference between the SPP wave vector k_{spp} and the wave vector of the flat wave k_0. This hinders the fulfillment of the condition of their matching, which leads to larger energy losses of the incident wave at diffraction on the sample edge. In addition, an increase in the diffraction losses can also be caused by the imperfection of the sample edge (its roundness and divergence from a straight line [53]).
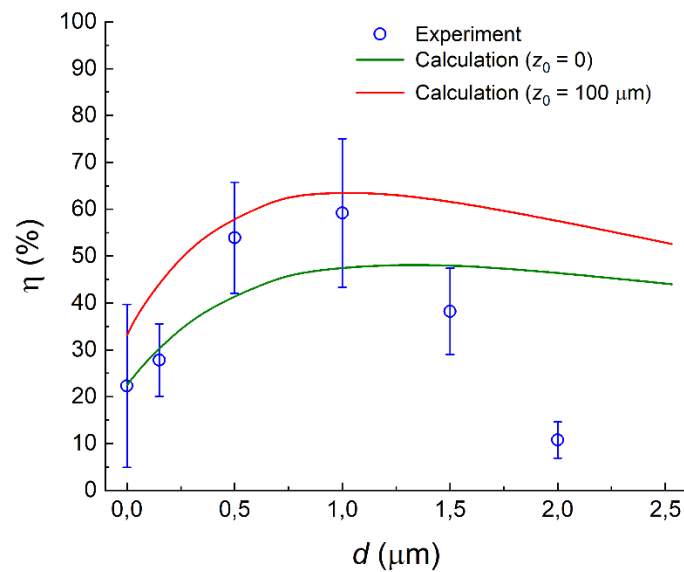
Figure 9. SPP generation efficiency η vs. ZnS coating layer thickness d, calculated by Formulas (10) and (11) with the use of attenuation coefficient experimental values α presented in Figure 8a (blue circles) and calculated dependences $\eta(d)$ at z_0 equal to 0 and 100 μm (see Figure 4a).

According to the calculations (see Figure 4), the maximum of the dependence $\eta(d)$ is reached at a slightly thinner ZnS layer ($d \approx 0.7$ μm) when the efficiency is close to 80% (20% higher than that in the experiment). This difference can be caused both by alignment inaccuracy in the search for the optimal position z_0 and by less probability of matching of the wave vectors of the incident wave and SPPs because of imperfection of the edge sample.

6. Conclusions

The paper demonstrates for the first time an experimental evaluation of the efficiency of SPP generation in the THz range ($\lambda_0 = 141$ μm) by the end-fire coupling technique with a sample in the form of the cylindrical segment, its convex surface metalized with a gold layer having a dielectric coating of zinc sulfide (ZnS) of thickness $d = 0$–2 μm. Such a form of sample makes it possible to spatially separate SPPs propagating over the convex surface of the sample from the parasitic bulk waves resulting from diffraction of the incident radiation on the edge of this surface and scattering of SPPs on the surface inhomogeneities. The imaging system recorded the intensity of the bulk radiation from the SPP track, and the SPP attenuation coefficients were found for different thicknesses d of the ZnS coating, which made it possible to determine the efficiency of THz SPP generation by the end-fire coupling technique. On the sample without a ZnS layer on the gold surface, the SPP generation efficiency η was about 20%. In the presence of a ZnS layer on the gold, the η value gradually increased with d, reached the maximum ($\eta_{max} \approx 60\%$) at $d \approx 1$ μm, and then gradually decreased. The calculated values of the efficiency η were in good agreement with the experiment at the coating thickness $0 < d < 1$ μm. However, at $d > 1$ μm, the experimental values of η went down faster than the calculated values. The reason for this discrepancy can be both the change in the diffraction conditions with increasing d and the imperfection of the sample edge. According to a theoretical analysis, the generation efficiency of THz SPPs can be increased to 80% or more via the selection of a suitable profile of intensity distribution in the cross section of the incident radiation beam and the optimal direction of the beam on the edge of the sample, as well as in the presence of a dielectric layer of a certain thickness on the metal.

Appendix A

The waist w of a beam focused by a cylindrical mirror was measured (Figure A1). A detector array Pyrocam IV was used for the detection of the focal spot because due to the absence of an input window in this detector, the interference effects were less manifested in the images. As can be seen, the minimum value of the waist of the Gaussian beam was approximately w_0 = 450 μm.
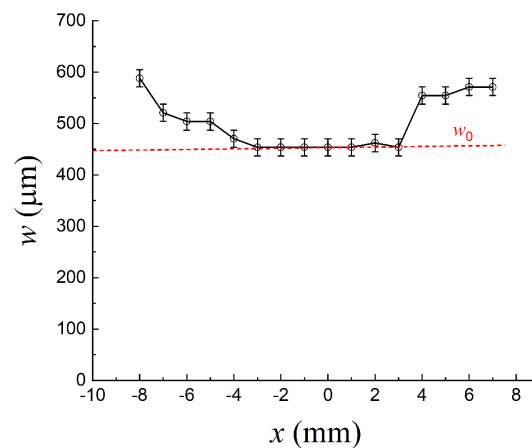

Figure A1. Waist of Gaussian beam focused on edge of cylindrical sample.

Appendix B

Figure A2 shows the scheme for estimation of the size of the SPP track section from which the bulk waves get to the detector array. The maximum arc length (in angular units) at which the bulk waves from the SPP track reach the detector is governed by the lens diameter D = 50.8 mm and its focal length f = 75 mm:

$$tg(\Delta\theta/2) \approx \frac{D/2}{2f} \tag{A1}$$

In our case, $\Delta\theta/2 \approx 0.166 = 9.6°$, i.e., the viewing angle of the imaging system corresponds to $\Delta\theta \approx 20°$.
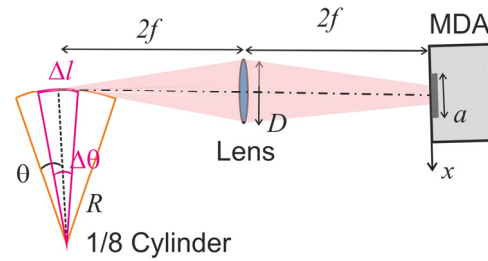
Figure A2. Optical scheme for estimation of SPP track area from which detector array gets bulk waves generated by SPPs on the curvature of the sample surface and surface inhomogeneities.

The range of angles $\Delta\theta_m/2$ at which the bulk radiation from the SPP track arrives at the detector array is determined by the size of the array. The $\Delta\theta_m/2$ value for specific conditions can be found via the thin-lens formula:

$$tg(\Delta\theta_m/2) \approx \frac{a/2}{R \cdot tg(\Delta\theta_m/2)} \tag{A2}$$

where R is the radius of the cylinder and a is the size of the array. Then the value of the angle sector within which the bulk radiation from the SPP track arrives at the detector array is

$$\Delta\theta_m/2 \approx arctg\left(\sqrt{\frac{a/2}{R}}\right) \tag{A3}$$

With the size of the detector element along the x-axis a = 16 mm, we get $\Delta\theta_m \approx 40°$, which is twice the value of $\Delta\theta$ obtained subject to the limitation by the lens size. This means that only half of the radiation flux breaking off the sample surface within the angle range $\Delta\theta_m$ hits the lens and, consequently, reaches the detector array. Thus, the viewing angle of the detector array is defined by the size of the lens, and only half of the array will be illuminated, which was observed in the experiment (see Figure 6a). The size of the SPP track segment from which the bulk radiation got onto the detector was equal to $\Delta l \approx R \cdot \Delta\theta \approx 1$ cm. With the SPP intensity strongly attenuating on the curvature of the sample surface, the main contribution to the recorded signal was made by the initial part of the segment Δl.

Appendix C

Figure A3 shows the calculated SPP dispersion curves ν (k_{spp}) for the three-layer Au-ZnS-air structures having a ZnS coating with thickness d = 0.0, 0.1, 0.5, 1.0, and 2.5 μm (solid lines). The gold permittivity ε_m was calculated by the Drude model with the use of the reference values of the plasma frequency ω_p = 1.37 × 10^{16} s^{-1} and frequency of the collisions of the conduction electrons ω_τ = 4.05 × 10^{13} s^{-1} [57]:

$$\varepsilon_m(\omega) = 1 - \frac{\omega_p{}^2}{\omega^2 + \omega_\tau{}^2} + i \cdot \frac{\omega_\tau \cdot \omega_p{}^2}{\omega \cdot (\omega^2 + \omega_\tau{}^2)}. \tag{A4}$$

where $\omega = 2\pi c/\lambda_0$ = 1.34 × 10^{13} s^{-1} (c is the speed of light in a vacuum). For reference, the free-wave dispersion curve ν (k_0) (dash black line) is shown.
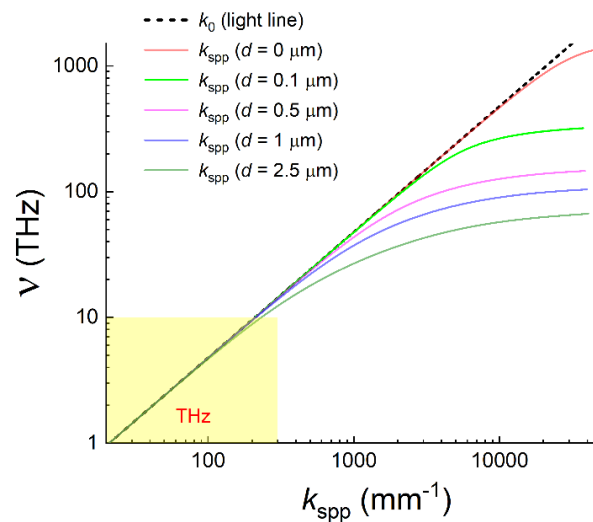
Figure A3. SPP dispersion curves ν (k_{spp}) for three-layer Au-ZnS-air structures having ZnS coating thickness d = 0.0, 0.1, 0.5, 1.0, and 2.5 μm (solid lines), calculated for Drude permittivity of gold; free-wave dispersion curve (dash black line).

References

1. Agranovich, V.M.; Mills, D.L. *Surface Polaritons: Electromagnetic Waves at Surfaces and Interfaces*; Modern Problems in Condensed Matter Sciences; Elsevier Science Pub. Co: Amsterdam, The Netherlands; New York, NY, USA, 1982; ISBN 978-0-444-86165-8.
2. Raether, H. *Surface Plasmons on Smooth and Rough Surfaces and on Gratings*; Springer Tracts in Modern Physics; Springer: Berlin/Heidelberg, Germany, 1988; Volume 111, ISBN 978-3-540-17363-2.
3. Maier, S.A. *Plasmonics: Fundamentals and Applications*; Springer: New York, NY, USA, 2007; ISBN 978-0-387-33150-8.
4. Liang, Y.; Koshelev, K.; Zhang, F.; Lin, H.; Lin, S.; Wu, J.; Jia, B.; Kivshar, Y. Bound States in the Continuum in Anisotropic Plasmonic Metasurfaces. *Nano Lett.* **2020**, *20*, 6351–6356. [CrossRef] [PubMed]
5. Gallerano, G.P.; Biedron, S. Overview of Terahertz Radiation Sources. In Proceedings of the 2004 FEL Conference, Comitato Conferenze Elettra, Trieste, Italy, 29 August–3 September 2004.
6. Sizov, F. Terahertz Radiation Detectors: The State-of-the-Art. *Semicond. Sci. Technol.* **2018**, *33*, 123001.
7. Begley, D.L.; Alexander, R.W.; Ward, C.A.; Miller, R.; Bell, R.J. Propagation Distances of Surface Electromagnetic Waves in the Far Infrared. *Surf. Sci.* **1979**, *81*, 245–251. [CrossRef]
8. Baragwanath, A.J.; Gallant, A.J.; Chamberlain, J.M. Terahertz Plasmonic Structures. In *Terahertz Spectroscopy and Imaging*; Peiponen, K.-E., Zeitler, A., Kuwata-Gonokami, M., Eds.; Springer Series in Optical Sciences; Springer: Berlin/Heidelberg, Germany, 2012; Volume 171, pp. 539–568. ISBN 978-3-642-29563-8.
9. Zhang, X.; Xu, Q.; Xia, L.; Li, Y.; Gu, J.; Tian, Z.; Ouyang, C.; Han, J.; Zhang, W. Terahertz Surface Plasmonic Waves: A Review. *Adv. Photon.* **2020**, *2*, 1. [CrossRef]
10. Koteles, E.S.; McNeill, W.H. Far Infrared Surface Plasmon Propagation. *Int. J. Infrared Milli. Waves* **1981**, *2*, 361–371. [CrossRef]
11. Steijn, K.W.; Seymour, R.J.; Stegeman, G.I. Attenuation of Far-Infrared Surface Plasmons on Overcoated Metal. *Appl. Phys. Lett.* **1986**, *49*, 1151–1153. [CrossRef]
12. Mills, D.L. Attenuation of Surface Polaritons by Surface Roughness. *Phys. Rev. B* **1975**, *12*, 4036–4046. [CrossRef]
13. Raether, H. Surface Plasmons and Roughness. In *Surface Polaritons*; Agranovich, V.M., Mills, D.L., Eds.; North-Holland Publishing Company: Amsterdam, The Netherlands, 1982; Chapter 9, pp. 331–403.
14. Zhizhin, G.N.; Moskalova, M.A.; Shomina, A.V.; Yakovlev, V.A. Surface Electromagnetic Wave Propagation on Metal Surfaces. In *Surface Polaritons*; Agranovich, V.M., Mills, D.L., Eds.; North-Holland Publishing Company: Amsterdam, The Netherlands, 1982; Chapter 3, pp. 93–144.
15. Sambles, J.R. Grain-Boundary Scattering and Surface Plasmon Attenuation in Noble Metal Films. *Solid State Commun.* **1984**, *49*, 343–345. [CrossRef]
16. Pandey, S.; Gupta, B.; Chanana, A.; Nahata, A. Non-Drude like Behaviour of Metals in the Terahertz Spectral Range. *Adv. Phys. X* **2016**, *1*, 176–193. [CrossRef]
17. Naftaly, M.; Dudley, R. Terahertz Reflectivities of Metal-Coated Mirrors. *Appl. Opt.* **2011**, *50*, 3201. [CrossRef]
18. Gerasimov, V.V.; Knyazev, B.A.; Nikitin, A.K.; Zhizhin, G.N. A Way to Determine the Permittivity of Metallized Surfaces at Terahertz Frequencies. *Appl. Phys. Lett.* **2011**, *98*, 171912. [CrossRef]
19. Pandey, S.; Liu, S.; Gupta, B.; Nahata, A. Self-Referenced Measurements of the Dielectric Properties of Metals Using Terahertz Time-Domain Spectroscopy via the Excitation of Surface Plasmon-Polaritons. *Photon. Res.* **2013**, *1*, 148. [CrossRef]

20. Gerasimov, V.V.; Nikitin, A.K.; Lemzyakov, A.G. Planar Michelson Interferometer Using Terahertz Surface Plasmons. *Instrum. Exp. Tech.* **2023**, *66*, 423–434. [CrossRef]

21. Ma, Y.; Nguyen-Huu, N.; Zhou, J.; Maeda, H.; Wu, Q.; Eldlio, M.; Pistora, J.; Cada, M. Mach–Zehnder Interferometer-Based Integrated Terahertz Temperature Sensor. *IEEE J. Select. Top. Quantum Electron.* **2017**, *23*, 4. [CrossRef]

22. Nikitin, A.K.; Khitrov, O.V.; Gerasimov, V.V.; Khasanov, I.S.; Ryzhova, T.A. In-Plane Interferometry of Terahertz Surface Plasmon Polaritons. *J. Phys. Conf. Ser.* **2019**, *1421*, 012013. [CrossRef]

23. Köhler, R.; Tredicucci, A.; Beltram, F.; Beere, H.E.; Linfield, E.H.; Davies, A.G.; Ritchie, D.A.; Iotti, R.C.; Rossi, F. Terahertz Semiconductor-Heterostructure Laser. *Nature* **2002**, *417*, 156–159. [CrossRef]

24. Williams, B.S. Terahertz Quantum-Cascade Lasers. *Nat. Photon* **2007**, *1*, 517–525. [CrossRef]

25. Wu, C.; Khanal, S.; Reno, J.L.; Kumar, S. Terahertz Plasmonic Laser Radiating in an Ultra-Narrow Beam. *Optica* **2016**, *3*, 734. [CrossRef]

26. Zhizhin, G.N.; Nikitin, A.K.; Rijova, T.A. Uncooled Metal Bolometer. Patent of the Russian Federation for the Invention No.2325729, Bulletin No.15, 27 May 2008.

27. Wang, Z.; Ishibashi, K.; Komiyama, S.; Nagai, N.; Hirakawa, K. Integrating a Plasmonic Coupler to Photo Detector of Terahertz Frequency. *Appl. Phys. Lett.* **2012**, *101*, 091114. [CrossRef]

28. Isaac, T.H.; Barnes, W.L.; Hendry, E. Determining the Terahertz Optical Properties of Subwavelength Films Using Semiconductor Surface Plasmons. *Appl. Phys. Lett.* **2008**, *93*, 241115. [CrossRef]

29. Liu, G.; He, M.; Tian, Z.; Li, J.; Liu, J. Terahertz Surface Plasmon Sensor for Distinguishing Gasolines. *Appl. Opt.* **2013**, *52*, 5695. [CrossRef] [PubMed]

30. Hailu, D.M.; Alqarni, S.; Cui, B.; Saeedkia, D. Terahertz Surface Plasmon Resonance Sensor for Material Sensing. In *Proceedings of SPIE—The International Society for Optical Engineering*; Cheben, P., Schmid, J., Boudoux, C., Chen, L.R., Delâge, A., Janz, S., Kashyap, R., Lockwood, D.J., Loock, H.-P., Mi, Z., Eds.; SPIE: Ottawa, ON, Canada, 2013; p. 89151G.

31. Bogomolov, G.D.; Zhizhin, G.N.; Nikitin, A.K.; Knyazev, B.A. Geodesic Elements to Control Terahertz Surface Plasmons. Nuclear Instruments and Methods in Physics Research Section A: Accelerators, Spectrometers, Detectors and Associated Equipment. *Science* **2009**, *603*, 52–55. [CrossRef]

32. Nazarov, M.M.; Bezus, E.A.; Shkurinov, A.P. Thin and Thick Dielectric Films for THz Surface Plasmon Control. *Laser Phys.* **2013**, *23*, 056008. [CrossRef]

33. Gerasimov, V.V.; Knyazev, B.A.; Lemzyakov, A.G.; Nikitin, A.K.; Zhizhin, G.N. Growth of Terahertz Surface Plasmon Propagation Length Due to Thin-Layer Dielectric Coating. *J. Opt. Soc. Am. B* **2016**, *33*, 2196. [CrossRef]

34. Sambles, J.R.; Bradbery, G.W.; Yang, F. Optical Excitation of Surface Plasmons: An Introduction. *Contemp. Phys.* **1991**, *32*, 173–183. [CrossRef]

35. O'Hara, J.F.; Averitt, R.D.; Taylor, A.J. Terahertz Surface Plasmon Polariton Coupling on Metallic Gratings. *Opt. Express* **2004**, *12*, 6397. [CrossRef]

36. Seymour, R.J.; Krupczak, J.J.; Stegeman, G.I. High Efficiency Coupling to the Overcoated Surface Plasmon Mode in the Far Infrared. *Appl. Phys. Lett.* **1984**, *44*, 373–375. [CrossRef]

37. Martl, M.; Darmo, J.; Unterrainer, K.; Gornik, E. Excitation of Terahertz Surface Plasmon Polaritons on Etched Groove Gratings. *J. Opt. Soc. Am. B* **2009**, *26*, 554. [CrossRef]

38. Nazarov, M.; Coutaz, J.-L.; Shkurinov, A.; Garet, F. THz Surface Plasmon Jump between Two Metal Edges. *Opt. Commun.* **2007**, *277*, 33–39. [CrossRef]

39. Zhang, R.; Guo, X.G.; Song, C.Y.; Buchanan, M.; Wasilewski, Z.R.; Cao, J.C.; Liu, H.C. Metal-Grating-Coupled Terahertz Quantum-Well Photodetectors. *IEEE Electron. Device Lett.* **2011**, *32*, 659–661. [CrossRef]

40. Zhang, R.; Shao, D.X.; Fu, Z.L.; Wang, H.X.; Zhou, T.; Tan, Z.Y.; Cao, J.C. Terahertz Quantum Well Photodetectors with Metal-Grating Couplers. *IEEE J. Select. Top. Quantum Electron.* **2017**, *23*, 4. [CrossRef]

41. Vaicikauskas, V.; Antanavicius, R.; Januskevicius, R. Efficiency of FIR Sew Excitation by Aperture, Prism, and Mesh Methods. *Int. J. Infrared Millim. Waves* **1999**, *20*, 447–452. [CrossRef]

42. Gerasimov, V.V.; Knyazev, B.A.; Nikitin, A.K. Wave-Vector Spectrum of Monochromatic Terahertz Surface Plasmon Polaritons on Real Surfaces. *Phys. Procedia* **2016**, *84*, 157–164. [CrossRef]

43. Saxler, J.; Gómez Rivas, J.; Janke, C.; Pellemans, H.P.M.; Bolívar, P.H.; Kurz, H. Time-Domain Measurements of Surface Plasmon Polaritons in the Terahertz Frequency Range. *Phys. Rev. B* **2004**, *69*, 155427. [CrossRef]

44. Yang, T.; Li, Y.; Stantchev, R.; Zhu, Y.; Qin, Y.; Zhou, X.; Huang, W. Detection of Defects on the Surface of a Semiconductor by Terahertz Surface Plasmon Polaritons. *Appl. Opt.* **2016**, *55*, 4139. [CrossRef]

45. Zhinzhin, G.N.; Yakovlev, V.A. Broad-band spectroscopy of surface electromagnetic waves. *Phys. Rep.* **1990**, *194*, 281–289. [CrossRef]

46. Zhinzhin, G.N.; Moskaleva, M.A.; Shomina, E.V.; Yakovlev, V.A. Search for the optimal conditions of prism conversion of surface electromagnetic waves in the IR region. *Opt. Spectrosc.* **1980**, *49*, 593–597.

47. Stegeman, G.I.; Wallis, R.F.; Maradudin, A.A. Excitation of Surface Polaritons by End-Fire Coupling. *Opt. Lett.* **1983**, *8*, 386. [CrossRef]

48. Hu, H.; Zeng, X.; Ji, D.; Zhu, L.; Gan, Q. Efficient End-Fire Coupling of Surface Plasmons on Flat Metal Surfaces for Improved Plasmonic Mach-Zehnder Interferometer. *J. Appl. Phys.* **2013**, *113*, 053101. [CrossRef]

49. Fisher, C.; Botten, L.C.; Poulton, C.G.; McPhedran, R.C.; De Sterke, C.M. End-Fire Coupling Efficiencies of Surface Plasmons for Silver, Gold, and Plasmonic Nitride Compounds. *J. Opt. Soc. Am. B* **2016**, *33*, 1044. [CrossRef]

50. Gerasimov, V.V.; Knyazev, B.A.; Nikitin, A.K.; Zhizhin, G.N. Experimental Investigations into Capability of Terahertz Surface Plasmons to Bridge Macroscopic Air Gaps. *Opt. Express* **2015**, *23*, 33448. [CrossRef] [PubMed]

51. Knyazev, B.A.; Gerasimov, V.V.; Nikitin, A.K.; Azarov, I.A.; Choporova, Y.Y. Propagation of Terahertz Surface Plasmon Polaritons around a Convex Metal–Dielectric Interface. *J. Opt. Soc. Am. B* **2019**, *36*, 1684. [CrossRef]

52. Grigoriev, I.S.; Meĭlikhov, E.Z. *Fizicheskie Velichiny: Spravochnik*; Ėnergoatomizdat: Moskva, Russia, 1991; ISBN 978-5-283-04013-4.

53. Tamir, T. (Ed.) *Integrated Optics*; Topics in Applied Physics; Springer: Berlin/Heidelberg, Germany, 1975; Volume 7, ISBN 978-3-662-43210-5.

54. Bell, R.J.; Alexander, R.W.; Ward, C.A.; Tyler, I.L. Introductory Theory for Surface Electromagnetic Wave Spectroscopy. *Surf. Sci.* **1975**, *48*, 253–287. [CrossRef]

55. Palik, E.D. *Handbook of Optical Constants of Solids (V.1)*; Academic Press: Cambridge, MA, USA, 2016; p. 824.

56. Gerasimov, V.V.; Nikitin, A.K.; Lemzyakov, A.G.; Azarov, I.A.; Kotelnikov, I.A. Obtaining the Effective Dielectric Permittivity of a Conducting Surface in the Terahertz Range via the Characteristics of Surface Plasmon Polaritons. *Appl. Sci.* **2023**, *13*, 7898. [CrossRef]

57. Ordal, M.A.; Long, L.L.; Bell, R.J.; Bell, S.E.; Bell, R.R.; Alexander, R.W.; Ward, C.A. Optical Properties of the Metals Al, Co, Cu, Au, Fe, Pb, Ni, Pd, Pt, Ag, Ti, and W in the Infrared and Far Infrared. *Appl. Opt.* **1983**, *22*, 1099. [CrossRef]

58. Arnaud, J.A. *Beam and Fiber Optics*; Elsevier Science: Amsterdam, The Netherlands, 2012; ISBN 978-0-323-14924-2.

59. Liu, J.; Liang, H.; Zhang, M.; Su, H. Metal Plate for Guiding Terahertz Surface Plasmon-Polaritons and Its Sensing Applications. *Opt. Commun.* **2015**, *339*, 222–227. [CrossRef]

60. Spesivtsev, E.V.; Rykhlitskii, S.V.; Shvets, V.A. Development of methods and instruments for optical ellipsometry at the institute of semiconductor physics of the Siberian branch of the Russian academy of sciences. *Avtometriya* **2011**, *47*, 5–12. [CrossRef]

61. Dem'yanenko, M.A.; Esaev, D.G.; Ovsyuk, V.N.; Fomin, B.I.; Aseev, A.L.; Knyazev, B.A.; Kulipanov, G.N.; Vinokurov, N.A. Microbolometer Detector Arrays for the Infrared and Terahertz Ranges. *J. Opt. Technol.* **2009**, *76*, 739. [CrossRef]

62. Dem'yanenko, M.A.; Esaev, D.G.; Knyazev, B.A.; Kulipanov, G.N.; Vinokurov, N.A. Imaging with a 90frames/s Microbolometer Focal Plane Array and High-Power Terahertz Free Electron Laser. *Appl. Phys. Lett.* **2008**, *92*, 131116. [CrossRef]